Scattering properties of protoplanetary dust analogs with microwave analogy: Aggregates of fractal dimensions from 1.5 to 2.8

Vanesa Tobon Valencia, Jean-Michel Geffrin, François Ménard, Julien Milli, Jean-Baptiste Renard, Hervé Tortel, Christelle Eyraud, Amelie Litman, Pascal Rannou, Maalouf Azar, et al.

To cite this version:

Vanesa Tobon Valencia, Jean-Michel Geffrin, François Ménard, Julien Milli, Jean-Baptiste Renard, et al.. Scattering properties of protoplanetary dust analogs with microwave analogy: Aggregates of fractal dimensions from 1.5 to 2.8. Astronomy & Astrophysics - A&A, 2022, 666, pp.A68. 10.1051/0004-6361/202142656 . hal-03837453

HAL Id: hal-03837453
https://hal.science/hal-03837453v1

Submitted on 12 Jul 2023

A&A 666, A68 (2022)
https://doi.org/10.1051/0004-6361/202142656

Astronomy
&
Astrophysics

Scattering properties of protoplanetary dust analogs with microwave analogy: Aggregates of fractal dimensions from 1.5 to 2.8

Vanesa Tobon Valencia[1], Jean-Michel Geffrin[1], François Ménard[2], Julien Milli[2], Jean-Baptiste Renard[3], Hervé Tortel[1], Christelle Eyraud[1], Amélie Litman[1], Pascal Rannou[4], Azar Maalouf[5], and Vincent Laur[5]

[1] Aix Marseille Univ, CNRS, Centrale Marseille, Institut Fresnel, Marseille, France
e-mail: `vanesa.tobon-valencia@fresnel.fr`
[2] Univ. Grenoble Alpes, CNRS, IPAG, 38000 Grenoble, France
[3] LPC2E, Université d'Orléans, CNRS, 45071 Orléans, France
[4] GSMA, Université de Reims, CNRS, 51687 Reims, France
[5] Lab-STICC, Université de Brest, CNRS, 29280 Brest, France

Received 12 November 2021 / Accepted 14 June 2022

ABSTRACT

Context. The growth of dust grains in protoplanetary disks is not understood in detail. Several studies have proposed the presence of aggregates and irregular grains to overcome the physical barriers in grain growth models. In order to understand the scattering properties of these aggregates, laboratory measurements of light scattering and microwave scattering have been developed over the last 50 years.

Aims. We aim to measure the scattering properties of different protoplanetary analog aggregates with fractal dimensions of 1.5, 1.7, 2.0, 2.5, and 2.8.

Methods. We used the microwave scattering technique (microwave analogy) for the measurements. The analog particles were virtually generated and fabricated by 3D printing with a controlled size (scaling factor), geometry, and refractive index. The seven analogs were measured at wavelengths ranging from 16.7 mm to 100 mm, leading to aggregate size parameters ranging from $X_{\mathrm{agg}} = 1$ to $X_{\mathrm{agg}} = 20$. The results were compared to finite element method calculations of the same analogs for cross-validation.

Results. The phase function and the degree of linear polarization were deduced from the scattered field measurements of the different aggregates. These scattering properties are compared and discussed as a function of the fractal dimension.

Conclusions. The scattering properties of aggregates with different fractal dimensions are different. Three different realizations of aggregates with the same fractal dimension but different monomer configurations yield the same phase functions. We verified that the maximum degree of linear polarization is higher for porous aggregates than for compact aggregates. Furthermore, the maximum polarization occurs at larger scattering angles for high fractal dimensions, while the half width at half maximum of the phase functions present larger values for small fractal dimensions.

Key words. protoplanetary disks – scattering – polarization – circumstellar matter – comets: general

1. Introduction

The processes by which dust grains from the interstellar medium evolve during the collapse of a molecular cloud and grow in a protoplanetary disk to form pebbles, boulders, and finally planetesimals or planets, are still subject to many open questions (see Testi et al. 2014, for a review). Several theoretical scenarios are proposed to overcome the physical barriers to grain growth, and many are tested in laboratory experiments (see Blum 2018, for a review). Fractal aggregates and irregular solid grains have been proposed as the outcome of the dust growth process and their presence was confirmed by the observations of cometary dust in the Solar System (e.g., Fulle & Blum 2017; Güttler et al. 2019, based on recent results from the Rosetta and previous missions). However, observational evidence for complex particles in protoplanetary disks is still missing, despite tremendous progress in high-angular resolution instruments in the (sub)millimeter, near-infrared, and optical wavelengths. Indeed, sensitive panchromatic observations of disks at high-angular resolution are now routinely produced by facilities such as ALMA, SPHERE, and GPI, but most interpretations do not consider aggregates and still rely on compact spherical particles. As a first step to providing more realistic tools to interpret protoplanetary disk observations and study grain growth in those disks, this paper presents a study of the scattering properties of small fractal dust aggregates made of 74 monomers.

Apart from their refractive index, aggregates are characterized by their porosity and their fractal dimension D_{f} as these two parameters are closely related Bertini et al. (2009). The fractal dimension D_{f} ranges from one for a very fluffy or porous particle, to three for a compact sphere. The size parameter $X_{\mathrm{agg}} = 2\pi R_{\mathrm{m}}/\lambda$ is another important descriptive parameter, where R_{m} is the radius of the sphere enclosing the aggregate and λ is the incident wavelength. These aggregate characteristics will directly influence their optical properties such as their scattering cross-sections, phase function, asymmetry parameter, degree of polarization, and albedo.

Laboratory experiments to characterize the scattering properties of aggregates have been carried out since the 1970s to study, for example, interplanetary dust particles, soot particles, and aerosols in planetary atmospheres. Two broad laboratory measurement techniques have been used: optical light scattering on samples, and microwave analogy techniques on scaled-up analogs.

The optical scattering experiments usually measure particles in the (sub)millimeter size range, and therefore with size parameters X_{agg} much larger than one. These particles can be ejected by an aerosol generator, leading to measurements taken for a cloud of particles (Volten et al. 2007; Muñoz et al. 2010). Particles large enough (millimeter-sized) can also be positioned on a holder and measured individually (Muñoz et al. 2020). Other light scattering instruments use levitation, with the advantage of accessing 4π measurements for single targets. One can cite, for example, ultrasonic levitation with acquisition with the 4π Scatterometer at visible wavelengths (Maconi et al. 2020), microgravity levitation during parabolic flights with the PROGRA^2 polarimeter for particles that are larger than 20 µm (Renard et al. 2014), and air levitation experiments, covering sizes from submicrons to tens of microns (Hadamcik et al. 2003).

Unfortunately, light scattering experiments are facing challenges. Uncontrolled aggregate geometries lead to measurement results that may be difficult to model in detail and interpret. Also, small-sized particles have a tendency to stick together during air ejection and levitation due to Van der Waals forces, making the measurement of individual isolated particles difficult (Renard et al. 2002).

Another way of obtaining scattering properties is to take advantage of the microwave analogy, which relies on the scale invariance rule (SIR). In Maxwell's equations, the SIR states that an electromagnetic system will give equivalent scattering results at any frequency if all geometrical dimensions are scaled in proportion, while keeping the complex refractive index identical (Gustafson 1996; Mishchenko et al. 2000; Mishchenko 2006). Some of the first particle analogs to be fabricated were inspired by stratospheric dust particles collected by high-altitude-flying U2 spy-planes (Brownlee 1979; Fraundorf 1980). These analogs were measured in the microwave scattering facility of Bochum University. They were fabricated with size parameters between $X_{\mathrm{agg}} = 20$ and $X_{\mathrm{agg}} = 32$ (Giese et al. 1978) to match the zodiacal light measured by the Helios and Pioneer space probes. However, the geometry of these analogs was not controlled.

Microwave measurements of the scattering phase function and degree of linear polarization of aggregates made of identical monomers followed: the assembly of spherical monomers with monomer size parameters ranging from $X_{\mathrm{mon}} = 0.58$ (Rayleigh scattering) to $X_{\mathrm{mon}} = 7.86$ (Zerull et al. 1993; Xu & Gustafson 1997, 2001); and the assembly of spherical, spheroidal and cylindrical monomers with monomer size parameters ranging from $X_{\mathrm{mon}} = 0.51$ to $X_{\mathrm{mon}} = 21.1$ (Gustafson & Kolokolova 1999; Thomas-Osip et al. 2005). The main conclusion of these early studies was that the more packed the aggregate, the wider the forward scattering peak of the phase function. Unfortunately, the fractal dimensions of these aggregates are unknown.

Scattering properties of protoplanetary aggregates can also be estimated by numerical simulations. More information can be found in, for example, Min et al. (2016); Tazaki et al. (2016); Tazaki & Tanaka (2018), where different scattering methods such as discrete dipole approximation (DDA), T-matrix, or approximated methods were used. Similarly, the scattering properties of interplanetary dust and cometary particles were studied by Kimura et al. (2016); Lasue & Levasseur-Regourd (2006); Lasue et al. (2007) and Halder et al. (2018), and atmospheric aerosols by Sorensen et al. (2017, 2018), and Liu & Mishchenko (2018).

Although several measurements and theoretical studies of the scattering properties of aggregates exist, the need remains for more results, in particular to differentiate between (fractal) aggregates and irregular polydisperse particles, as well as to study large particles of (sub)micrometer size and aggregates containing thousands of monomers with a realistic size distribution (Kolokolova et al. 2004). The aim of this paper is, therefore, to provide laboratory measurements, using the microwave scattering technique, of the scattering properties of protoplanetary dust aggregates whose fractal dimensions, geometries, and refractive indices are fully controlled. Together with these measurements, we also provide finite element method (FEM) simulations of the same aggregate particles for cross validation.

The present paper thus studies, numerically and experimentally, the scattering properties, namely the phase function and degree of linear polarization, of seven different protoplanetary analog aggregates with wavelengths ranging from 16 mm to 100 mm (in frequency, from 3 GHz to 18 GHz), leading to size parameters ranging from $X_{\mathrm{agg}} = 1$ to $X_{\mathrm{agg}} = 20$. The measured scattered amplitude and phase of the scattered fields are transformed into phase functions and degrees of polarization (more commonly used in astronomy) by averaging multiple orientations of the aggregates. These aggregates are defined by their fractal dimensions D_{f} of 1.5, 1.7, 2.0, 2.5, and 2.8. The geometry and the refractive index are controlled to high accuracy, thanks to additive manufacturing techniques (Vaillon & Geffrin 2014), which have proved to be more versatile than the monomer-to-monomer gluing used previously by Sabouroux et al. (2007), Merchiers et al. (2009), and Merchiers et al. (2010).

The paper is organized as follows. Section 2 describes the dust analog aggregates. Section 3 describes the experimental setup and measurement procedure. Section recalls the definitions of the two scattering properties of interest: phase function and degree of linear polarization, while Sect. 5 describes the numerical simulation set-up. Section 6 presents the measurement results and a comparison between measurements and simulations, and Sect. 7 presents the conclusions and prospects for future work.

2. Analogs of dust aggregates

The evolution of dust particles in protoplanetary disks is complex and involves several processes. The structure and shape of a particle can retain the record of its evolution, in particular its collisional history. Yet, very little direct information is available on the particle structures and shapes in disks, and observing these signatures would significantly further our understanding of dust evolution. To do so, one must first understand the typical signatures of different families of particles. In this paper we will focus on fractal aggregates.

We generated seven different types of aggregates with fractal dimensions ranging from 2.8 (compact) to 1.5 (fluffy, porous); see Eq. (1) and Table 1. This range of fractal dimensions covers the outcome of dust growth by collisions of individual monomers with clusters and of collisions between clusters. For comparison, ballistic particle-cluster aggregation (BPCA) results in aggregates with high fractal dimensions, typically larger than 2.5, while ballistic cluster-cluster aggregation (BCCA) yields objects with fractal dimensions typically smaller than 2 (Meakin 1984) for slow collisional velocities.

To produce these analogs, two steps were necessary: first, their virtual generation, and second, 3D printing. The details for these two steps are described in the following subsections.

Table 1. Analog aggregate properties with monomer size parameter from $X_{\mathrm{mon}} = 1.04$ ($\lambda = 16.7$ mm) to $X_{\mathrm{mon}} = 0.17$ ($\lambda = 100$ mm).

Aggregate	Aggregate technical name	Numerical fractal dimension	Radius of gyration (mm)-R_{g}	Radius of the circumscribed sphere (mm)-R_{m}	Size parameter of the aggregate $\lambda = 16.7$ mm to $\lambda = 100$ mm	Porosity % -$P_{R_{\mathrm{g}}}$	Material packing density-ρ
AgC232	Ag_DLA_Df1.5_N74	1.5	32.30	51.98	19.60 to 3.27	97.91	0.011
AgC233	Ag_DLA_Df1.7_N74	1.7	23.92	36.58	13.80 to 2.30	94.90	0.031
AgC185	Ag_DLA_Df2.0_N74_1	2.0	17.03	26.20	9.88 to 1.65	85.68	0.085
AgC2211	Ag_DLA_Df2.0_N74_2	2.0	17.03	26.54	10.01 to 1.67	85.83	0.081
AgC2221	Ag_DLA_Df2.0_N74_3	2.0	17.03	26.00	9.81 to 1.63	85.83	0.086
AgC186	Ag_DLA_Df2.5_N74	2.5	11.60	18.19	6.86 to 1.14	54.78	0.252
AgC187	Ag_DLA_Df2.8_N74	2.8	9.83	15.49	5.84 to 0.97	25.88	0.407

2.1. Virtual generation

Nature uses different types of aggregation, giving birth to a variety of different fractal dimensions as previously explained. To generate a large range of fractal dimensions, all aggregates were generated with a tunable diffusion limited aggregation software (DLA) created by Wozniak et al. (2012), in which, at each monomer-cluster aggregation scheme, the algorithm verifies if the fractal dimension is correct. If it is not correct, the monomer is eliminated and another monomer will diffuse toward the seed. Thus, this software is able to produce different fractal dimensions that are present in nature because of BPCA and BCCA.

Three input parameters are necessary to describe the particles: the fractal dimension of the aggregate, the number of monomers included in the particle, and the radius of the monomers. All monomers are spherical and for this paper they have the same size (they are monodisperse). Based on the fractal equation, these parameters are related as follows:

$$N = k_0 (R_{\mathrm{g}}/a)^{D_{\mathrm{f}}}, \tag{1}$$

where N is the number of monomers, k_0 the fractal prefactor (or proportionality constant), R_{g} the gyration radius (which is the mean-squared of the distances between the aggregate center of mass and the geometric center of each monomer), a the monomer radius, and D_{f} the fractal dimension.

All aggregates were fabricated with $N = 74$ monomers, each with a radius $a = 2.5$ mm. The software assumes a single point of contact between each monomer (i.e., no overlapping). The fractal prefactor is set to $k_0 = 1.593$. This prefactor value, which depends on the compactness factor and the fractal dimension of the particle (see Eq. (16) of Sorensen & Roberts 1997), is set as constant in the DLA software. Specific information of each aggregate is given in Table 1.

In Fig. 1 and Table 1, the names of analogs are made of a string specifying first that they are aggregates generated with DLA (Ag_DLA), followed by their fractal dimension (Df) and the number of monomers (N). When several realizations with the same parameters are made, an additional index is added at the end (see e.g., aggregates of fractal dimension $D_{\mathrm{f}} = 2$, where the index goes from one to three; Ag_DLA_Df2.0_N74_*index*). In Renard et al. (2021), we used a different naming convention. The names used in that paper are recalled in the first column of Table 1 for reference.

The values for the numerical fractal dimensions are also given in Table 1, as well as the radius of gyration (which was calculated by the software). Other parameters are the radius of the circumscribed sphere R_{m} (the smallest sphere inside which each aggregate fits), and the size parameter of each aggregate X_{agg}, which was calculated with the radius of the circumscribed sphere at the minimum and maximum wavelengths. Moreover, the porosity, $P_{R_{\mathrm{g}}}$, was estimated as the subtraction of unity from the ratio between the volume of the material in the aggregate and the volume of a sphere calculated with the radius of gyration. The values are in Table 1 (see Bertini et al. 2009, for definition of porosity in Eq. (7)). Finally, the material packing density, ρ, was calculated and defined as the ratio of the aggregate volume to the total volume of the circumscribed sphere (taken by Zubko et al. 2015).

2.2. 3D printing

After the virtual generation, aggregates were fabricated using an additive manufacturing process named stereolithography (SLA), which has the advantage of its good accuracy and surface finish compared to other 3D printing methods (the first time our group used this technique to print aggregates is in Vaillon & Geffrin 2014). The principle of SLA is to photopolymerize the liquid acrylic resin, layer by layer, and the solidification is performed using a UV laser. The resin that was used to print aggregates had a refractive index of $1.7 + i0.03$, which is close to the index of astronomical silicate without any metallic or mineral inclusions. Draine and Lee astronomical silicate has similar values from $\lambda = 0.2$ to 3 µm (for more information see Draine & Lee 1984).

It is important to note that the monomer radius used by the DLA software was different from the one chosen at the moment of the printing. The virtual generation of aggregates was at one point of contact between monomers, but printing monomers with this condition is not possible because there is no mechanical strength. For this reason, the monomer radius was increased by 10%, and thus the actual radius used in practise to allow the overlapping was $a_{\mathrm{int}} = a * 1.1$. Figure 1 presents a zoomed image of the interpenetration between two monomers (Fig. 1a) and Figs. 1b to h pictures of the printed aggregates.

3. Experimental setup and measurements

Measurements were performed in the anechoic chamber of the Centre Commun de Ressources en Micro-Ondes in Marseille, at wavelengths between 100 mm to 16 mm (corresponding to frequencies of 3 GHz to 18 GHz). Emitter and receiver antennas were used at the same states of polarization, horizontal and then vertical, which means that both were linearly polarized. Two types of configurations were used during measurements: forward and backward configurations, which corresponded to scattering angles (θ) from 0° to 130° in the horizontal system, and from 120° to 168° in the vertical system, respectively (Geffrin et al. 2012).

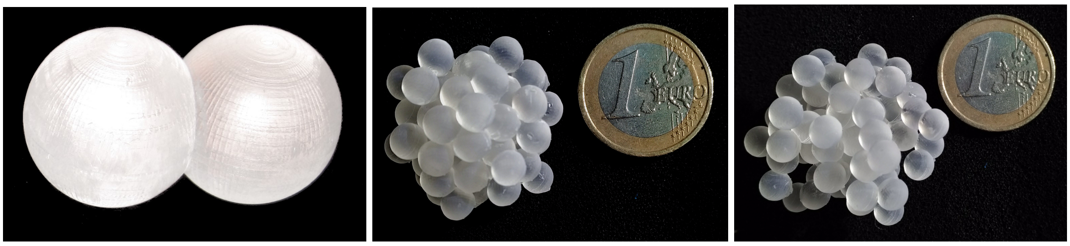

(a) Overlapping monomer (b) Ag_DLA_Df2.8_N74 (c) Ag_DLA_Df2.5_N74

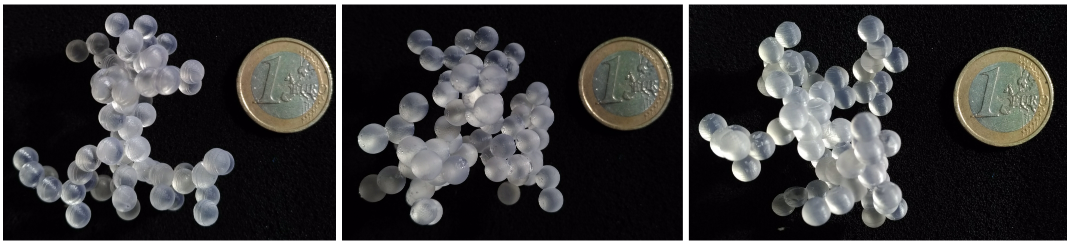

(d) Ag_DLA_Df2.0_N74_1 (e) Ag_DLA_Df2.0_N74_2 (f) Ag_DLA_Df2.0_N74_3

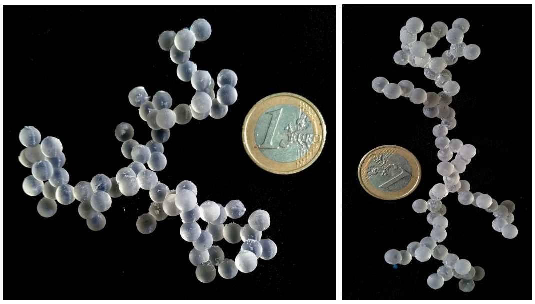

(g) Ag_DLA_Df1.7_N74 (h) Ag_DLA_Df1.5_N74

Fig. 1. 3D printed aggregates with their corresponding technical name.

3.1. Forward scattering zone: Experimental setup

Each analog was laid on an expanded polystyrene mast (transparent material for the used wavelengths) that was rotated all around its symmetry axis, 360°, so that each sample could be placed into different positions, giving multiple orientations. For a defined position, the receiving antenna was moved in the forward zone in the equatorial plane from $\theta = 130°$ to $-130°$, and then the polystyrene mast (in which the analog was placed) was turned 10° to restart the receiver antenna measurements with the horizontal system. Additionally, the emitter antenna was always positioned at the same place of the vertical system at $\Phi = 90$ (see Fig. 2).

3.2. Backward scattering zone: Experimental setup

The samples were similarly laid on a polystyrene mast that was turned all around its symmetry axis, 360°, as was done for the forward scattering experimental setup. The difference was the position of the receiver antenna, so that each experimental setup was used at different moments. In this case, the emitter antenna was placed at the same point of the vertical system but the receiver antenna was moved through the vertical system (from $\Phi = -11°$ to $\Phi = 78°$ and from $\Phi = 102°$ to $\Phi = 168°$ in the backward zone) for each 10° of rotation of the polystyrene mast (see Fig. 3).

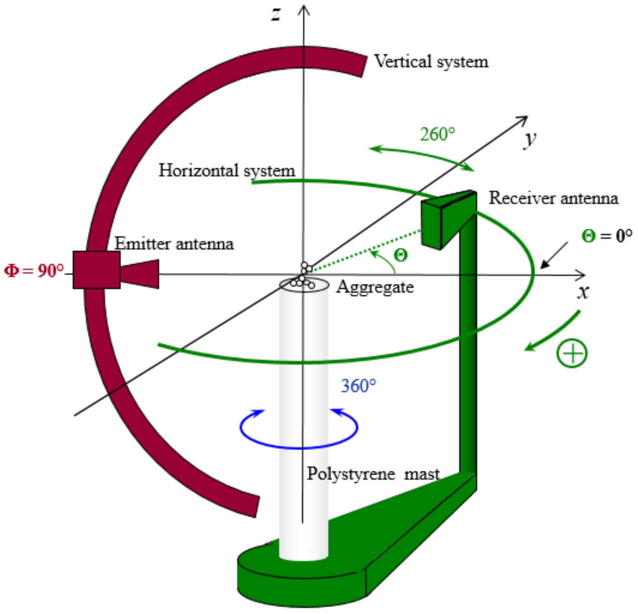

Fig. 2. Forward experimental setup where the emitter antenna is fixed at the vertical system while the receiver antenna moves on the horizontal system.

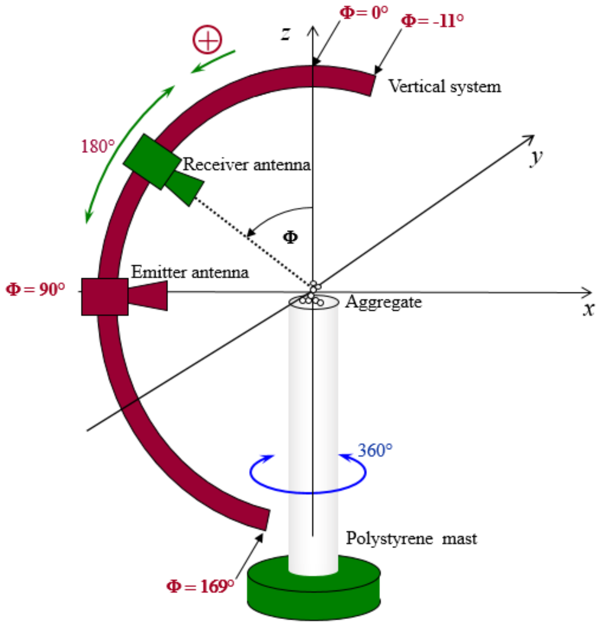

Fig. 3. Backward experimental setup where the emitter antenna is also fixed while the receiver antenna moves on the vertical system.

3.3. Measurements

Compact aggregates (in our case, fractal dimensions of 2.5 and 2.8), and fluffy aggregates (in our case, fractal dimensions of 2.0, 1.7, and 1.5) needed at least around 70 ± 10 orientations of each aggregate to obtain an averaged measurement of a randomly oriented object with an accuracy of 1.5% for the scattering phase function. For the degree of linear polarization, 60 ± 10 minimum orientations were needed, with an accuracy of 1% (see Renard et al. 2021, for more information).

The receiver antenna measured two different complex transmission coefficients to finally obtain the scattered field: the first one, where there was no sample, the second one, where there was the presence of a sample. Measurements were later calibrated with a metallic sphere measurement, turning the transmission values in incident field values (without the sample) and total field values (with the sample). This calibration can be summarized as considering an illumination of magnitude 1 and phase 0° at the center of the object. After obtaining the electric fields, drift errors were treated with a drift correction procedure (Eyraud et al. 2006; Bucci & Franceschetti 1987), applying a complex correction coefficient to the total field, and so the subtraction between the total field and the incident field was made, giving the scattered field, $\mathbf{E}_\mathrm{s} = \mathbf{E}_\mathrm{t} - \mathbf{E}_\mathrm{i}$.

Additionally, another post-processing procedure was applied in the form of an angular low pass filter (Bucci & Franceschetti 1987). This uses the deduction of the spatial bandwidth of the scattered field with two elements: the wave vector and the circumscribed sphere.

Finally, after obtaining the post-processed scattered values, the averaged intensities of the Jones matrix elements could be calculated. Knowing that the antennas were configured either in horizontal or vertical polarization, and supposing that cross polarizations are negligible, which was confirmed with simulations (see Fig. B.1), the only two Jones matrix elements that could be calculated were the co-polarized elements, S_1 and S_2. Based on these two elements, the phase function and the degree of linear polarization were calculated (see Sect. 4).

4. Scattering theory

After calculating the incident and scattered fields from transmission measurements, the following equation can be used to calculate the Jones matrix elements (Bohren & Huffman 1983):

$$\begin{pmatrix} E_{\parallel s} \\ E_{\perp s} \end{pmatrix} = \frac{e^{ik(r-z)}}{-ikr} \begin{pmatrix} S_2 & S_3 \\ S_4 & S_1 \end{pmatrix} \begin{pmatrix} E_{\parallel i} \\ E_{\perp i} \end{pmatrix}, \tag{2}$$

where $E_\parallel$ and $E_\perp$ are the complex amplitudes of incident ($_\mathrm{i}$) and scattered ($_\mathrm{s}$) fields, k is the wave number, z is the distance from the source to the object (emission distance), and r the distance from the object to the detector (detection distance). S_1, S_2, S_3, and S_4 are the elements of the Jones matrix, S_1 and S_2 being co-polarized elements, and S_3 and S_4 being cross-polarized elements.

These elements are related to the Mueller matrix elements (presented in Eq. (3)) by 16 equations described in Bohren & Huffman (1983).

$$\begin{pmatrix} I_\mathrm{s} \\ Q_\mathrm{s} \\ U_\mathrm{s} \\ V_\mathrm{s} \end{pmatrix} = \frac{1}{k^2 r^2} \begin{pmatrix} S_{11} & S_{12} & S_{13} & S_{14} \\ S_{21} & S_{22} & S_{23} & S_{24} \\ S_{31} & S_{32} & S_{33} & S_{34} \\ S_{41} & S_{42} & S_{43} & S_{44} \end{pmatrix} \begin{pmatrix} I_\mathrm{i} \\ Q_\mathrm{i} \\ U_\mathrm{i} \\ V_\mathrm{i} \end{pmatrix}, \tag{3}$$

where I, Q, U, and V are the Stokes parameters, and S_{ij} the elements of the Mueller matrix. The latter are used in our case to calculate two parameters: the phase function and the degree of linear polarization. The phase function is the element S_{11} and it is related to the Jones matrix elements by the following equation:

$$S_{11} = \frac{1}{2}\left(|S_1|^2 + |S_2|^2 + |S_3|^2 + |S_4|^2\right), \tag{4}$$

and the degree of linear polarization is:

$$\frac{-S_{12}}{S_{11}} = \frac{-\left(|S_2|^2 - |S_1|^2 + |S_4|^2 - |S_3|^2\right)}{\left(|S_1|^2 + |S_2|^2 + |S_3|^2 + |S_4|^2\right)}. \tag{5}$$

Assuming a macroscopically isotropic and symmetric medium (Mishchenko et al. 2000), and supposing random orientation of noninteracting particles, the Mueller matrix (Eq. (3)) can be simplified as follows:

$$\begin{pmatrix} I_\mathrm{s} \\ Q_\mathrm{s} \\ U_\mathrm{s} \\ V_\mathrm{s} \end{pmatrix} = \frac{1}{k^2 r^2} \begin{pmatrix} S_{11} & S_{12} & 0 & 0 \\ S_{12} & S_{22} & 0 & 0 \\ 0 & 0 & S_{33} & S_{34} \\ 0 & 0 & -S_{34} & S_{44} \end{pmatrix} \begin{pmatrix} I_\mathrm{i} \\ Q_\mathrm{i} \\ U_\mathrm{i} \\ V_\mathrm{i} \end{pmatrix}, \tag{6}$$

where elements S_{11} and S_{12} are present, thereby calculus of the phase function and degree of linear polarization is possible.

Based on Eq. (6) and knowing that the incident light coming from the star is nonpolarized, the phase function is simplified as:

$$S_{11} = \frac{1}{2}\left(|S_1|^2 + |S_2|^2\right), \tag{7}$$

and the degree of linear polarization (DOP), as:

$$P_\mathrm{s} = -\frac{S_{12}}{S_{11}} = \frac{|S_1|^2 - |S_2|^2}{|S_1|^2 + |S_2|^2}. \tag{8}$$

Our measurements have the same order of magnitude as if they were measured with nonpolarized light. For this reason, Appendix A explains why it is possible to obtain the phase function and degree of linear polarization for nonpolarized light based on our polarized measurements.

5. Simulation

Simulations were made based on two rigorous methods: the finite element method (FEM, Voznyuk et al. 2015) and the method of moment (MoM, Merchiers et al. 2010), using homemade codes. The simulations of the aggregates were performed using the same geometric file of the 3D object as the one used for 3D printing.

Our codes were previously compared to other methods like the superposition T-Matrix method (Mackowski & Mishchenko 1996) and DDA (Draine & Flatau 1994). In Merchiers et al. (2010) measurements and models like the superposition T-matrix method, DDA and MoM were compared in amplitude and phase of the scattered field of an aggregate, giving comparable results for different frequencies or wavelengths. Later, in Saleh et al. (2017), measurements and simulations of the scattered field of spheroids made in T-matrix and FEM also gave equivalent results in terms of intensity and phase. These results proved the validation of our simulation methods compared to other models and our measurements.

For the FEM, the weak form of the vector Helmholtz equation was used to compute the electromagnetic field. A scattered field formulation was implemented and the electric field was discretized onto basis functions associated with edges of tetrahedrons resulting from the unstructured mesh of the domain (Voznyuk et al. 2015). With a discretization of an order of $\lambda/10$ we obtained typically around a 2×10^6 degree of freedom (d.o.f.), and the sparse linear system obtained was solved thanks to dedicated sparse linear solvers like MUMPS in Amestoy et al. (2000) or Pardiso in Schenk & Gärtner (2011). The far field was then computed with the help of a classical near field to far field transformation.

On the other hand, the MoM solved the scattered field based on the observation equation which is a triple integral of the 3D domain in terms of: the free-space dyadic Green function, the contrast, which is the difference between the square of the wave number at a determined point and the square of the wave number in the vacuum, and the total field. Then the field inside the object, which is expressed as the addition between the incident and coupling term was computed with the coupling equation (Merchiers et al. 2010). It was numerically resolved with a 1D-FFT-method, exploiting the block-Toeplitz structure of the free-space dyadic Green function (Eyraud et al. 2020).

Both methods have advantages and disadvantages. For example, for the simulation of Ag_DLA_Df2.0_N74_1, MoM needs less memory (2GB) but more running time (from 1 h to 2 h depending on the frequency). On the contrary, FEM is faster (10 min for each frequency) but the needed memory is 70GB. Despite these differences, in terms of results, both methods gave very similar phase functions and DOP, as can be seen in Fig. B.2. Based on these consistent results, we decided to choose only one of them, which was the FEM, based on its better discretization of the scatterer (aggregates composed of spheres) in tetrahedrons and not in cubes, as done in the MoM.

6. Results and discussion

All results of phase function and DOP of aggregates were obtained by averaging the different values of the same aggregate at random orientations. This means that we first averaged the total intensity phase function $\langle S_{11} \rangle$ and the polarized intensity phase function $\langle S_{12} \rangle$ before dividing one by the other to find the average DOP $\frac{-\langle S_{12} \rangle}{\langle S_{11} \rangle}$. In the case of the DOP, the average was calculated before the division because the observables (S_{12} and S_{11}) in protoplanetary disks are already averaged in terms of orientation. It is important to note that in this study there is not an average on the size distribution, and all aggregates had the same monodispersity but with different fractal dimensions.

Table 2. Analog sizes conversion at different wavelengths.

Range name	Wavelength	Radius of monomer
Optical	400–700 nm	11–115 nm
NIR	1.00–2.50 µm	0.028–0.412 µm
Millimeter	0.30–2.60 mm	0.008–0.428 mm

The measurements were performed at wavelengths ranging from 16.7 mm to 100 mm. Knowing that the actual monomer radius is $a_{\mathrm{int}} = 2.75$ mm, the monomer size parameter ranges from 1.04 to 0.17. The monomer radius corresponding to the same size parameter at optical, NIR (1 µm to 2, 5 µm) or millimeter (ALMA band 3–10) wavelengths is shown in Table 2.

6.1. General analysis of phase function and DOP

Based on measurements, values of phase function and DOP were obtained for all samples in the forward zone and only for the aggregate Ag_DLA_Df2.0_N74_1 in the backward zone (for more information see database `https://www.fresnel.fr/EMSCOP/`). An example of these two parameters, in forward and backward zones, is illustrated in Fig. 4. To retrieve the mean scattering properties of our aggregates, we measured these properties with the necessary number of orientations for each aggregate, obtaining an even better accuracy of convergence, as previously mentioned, of 1% for the phase function and 0.5% for the DOP (according to Renard et al. 2021). For this reason, the scattered field of all our aggregates had 72 orientations, except for Ag_DLA_Df1.7_N74 and Ag_DLA_Df1.5_N74, which had 108 orientations each.

6.1.1. Behaviors of phase function and DOP for different fractal dimensions

The phase function in Fig. 4 shows good continuity between forward and backward measurements, near 120°. The levels of phase functions are coherent with size parameters. Indeed, higher values of size parameters represent higher cross-section $Q_{\mathrm{sca}}\pi a^2$, and thus a larger intensity of scattered light.

The measured phase functions presented here are calibrated, and thus their quantitative value is significant. Simulations and measurements have the same absolute values and curve shape, being both directly comparable (for a quantitative comparison see Appendix C). Nonetheless, backscattering measurements at angles higher than 160° are perturbed by filtering effects. Consequently, backscattering measurements are plotted up to 160°, and not 168° (in Fig. 4).

The forward-scattering peak of the phase function is a proper characteristic of the overall dimension of the aggregate and demonstrates how constructive interference dominates compared to other bumps (as it was shown by Zerull et al. 1993). These bumps represent the distribution of matter or structural information within the aggregates, if they are still there after averaging enough the orientation of the aggregate (Zerull et al. 1993). This demonstrates that, if the aggregate has a fractal dimension closer to three, a sphere, its distribution of matter is symmetric and so the bumps will be well-defined, representing constructive interference at the same scattering angles. This can

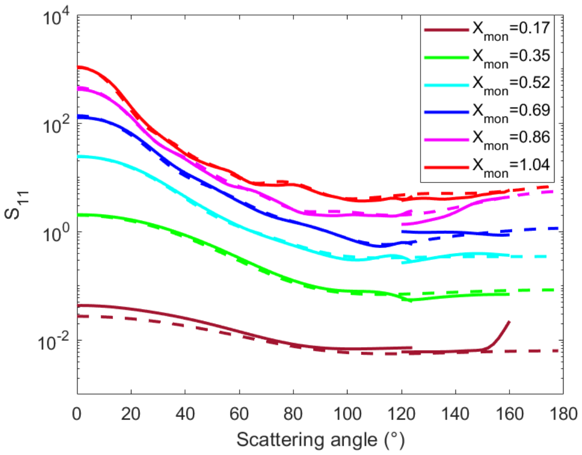

(a) Phase function

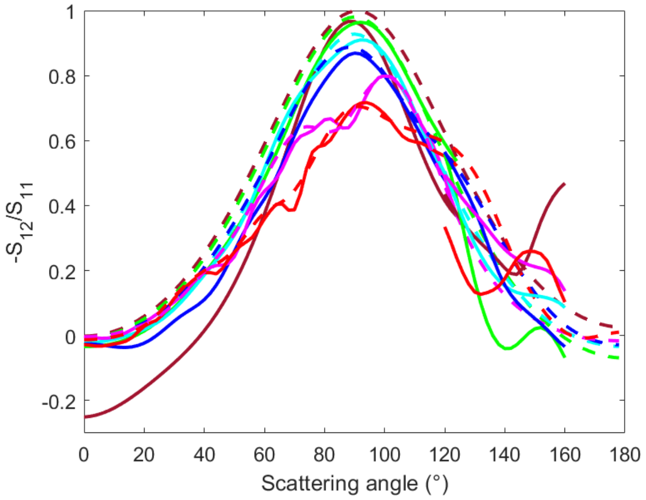

(b) Degree of linear polarization

Fig. 4. Measurements in the forward and backward zones (solid lines) and simulations (dashed lines) of Ag_DLA_Df2.0_N74_1 from $X_{\rm mon}$ = 0.17 to $X_{\rm mon}$ = 1.04.

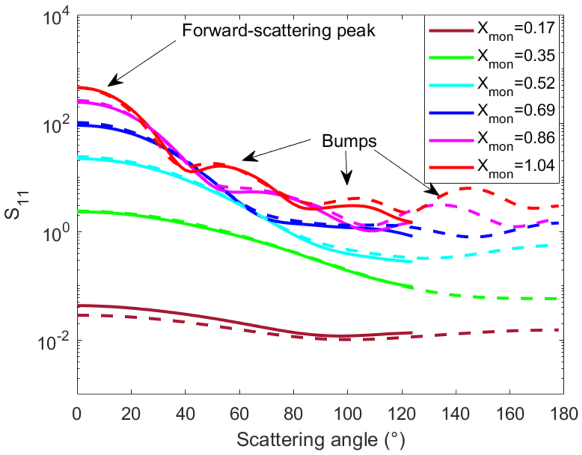

(a) Phase function

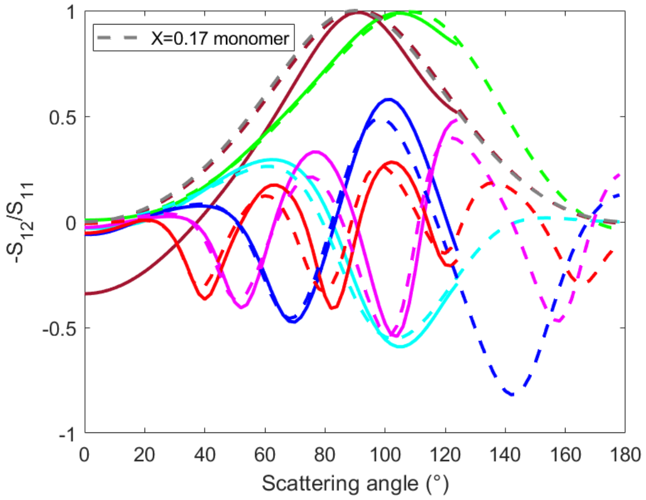

(b) Degree of linear polarization

Fig. 5. Measurements (solid lines) and simulations (dashed lines) of Ag_DLA_Df2.8_N74, from $X_{\rm mon}$ = 0.17 to $X_{\rm mon}$ = 1.04.

be seen in Fig. 5 for Ag_DLA_Df2.8_N74, which has almost the same fractal dimension as a sphere. It is important to notice that, as all of our aggregates have the same refractive index for a given monomer size parameter, changes in the phase function are entirely attributable to changes in the structure of the whole aggregate. For this reason, when $X_{\rm mon} \ll 1$ (Rayleigh regime), such as $X_{\rm mon}$ = 0.17, our aggregates are small compared to the wavelength and so the polarization is similar for all aggregates (as it can be seen in Fig. 10).

In addition, the DOP of Ag_DLA_Df2.0_N74_1 presents good continuity between forward and backward scattering measurements except for $X_{\rm mon}$ = 1.04. Simulations and forward measurements are similar except for $X_{\rm mon}$ = 0.17 from 0° to 70° because here the aggregate is very small compared to the wavelength, and thus is a really low scatterer, reaching the sensitivity limits of our experiments. In terms of backscattering, due to filtering side effects and to the lower accuracy of this configuration, $X_{\rm mon}$ = 0.17, $X_{\rm mon}$ = 0.35, and $X_{\rm mon}$ = 1.04 measurements have some enhancements around 160°.

At 90° there is a maximum around one for $X_{\rm mon}$ = 0.17 and $X_{\rm mon}$ = 0.35, and for the rest of monomer size parameters, the polarization peak levels are around 0.9–0.7. This phenomenon of Rayleigh-like behavior was also seen by Gustafson & Kolokolova (1999); Volten et al. (2007); Min et al. (2016); Liu & Mishchenko (2018), being the main cause the small size of constituent particles or monomers compared to the wavelength (subwavelength monomers). In this case all $X_{\rm mon} < 1$, except for $X_{\rm mon}$ = 1.04 in which the bell-shape is deformed. DOP illustrated in Fig. 5 shows that the FEM simulation of this aggregate at $X_{\rm mon}$ = 0.17 (brown dashed line) and the Mie simulation of the monomer (gray dashed line) have the exact same behavior. Notice that both dashed lines are superposed.

The phase function of Ag_DLA_Df2.8_N74 (see Fig. 5) has defined peaks and valleys at high $X_{\rm mon}$ for the forward-scattering peak and bumps. A possible explanation is that at $X_{\rm mon}$ = 1.04, $X_{\rm mon}$ = 0.86, and $X_{\rm mon}$ = 0.69, the monomer size is about the same size as the wavelength and the aggregate size parameter is about five to four times the wavelength. Hence, the whole aggregate size is close to λ and so the behavior would be that of Mie scattering. On the contrary, size parameters from $X_{\rm mon}$ = 0.17 to $X_{\rm mon}$ = 0.52 only have the forward-scattering peak, corresponding to aggregate size parameters of $X_{\rm agg}$ = 0.97 to $X_{\rm agg}$ = 2.92. As the size of the whole aggregate has

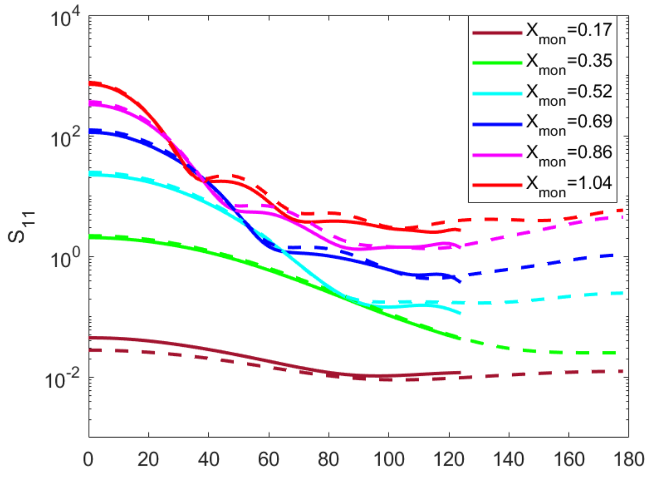

(a) Phase function

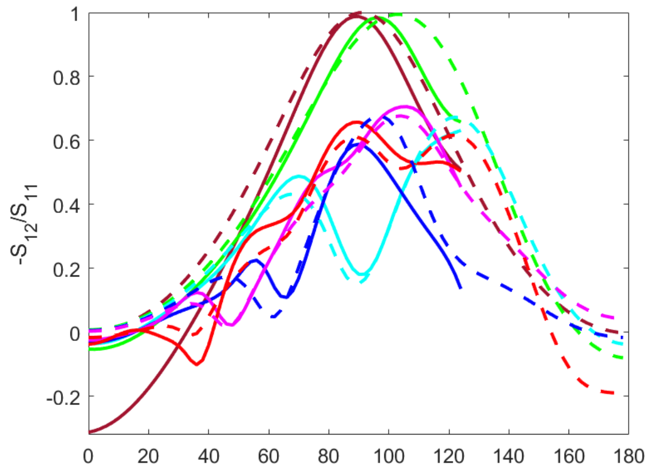

(b) Degree of linear polarization

Fig. 6. Measurements (solid lines) and simulations (dashed lines) of Ag_DLA_Df2.5_N74, from $X_{\mathrm{mon}} = 0.17$ to $X_{\mathrm{mon}} = 1.04$.

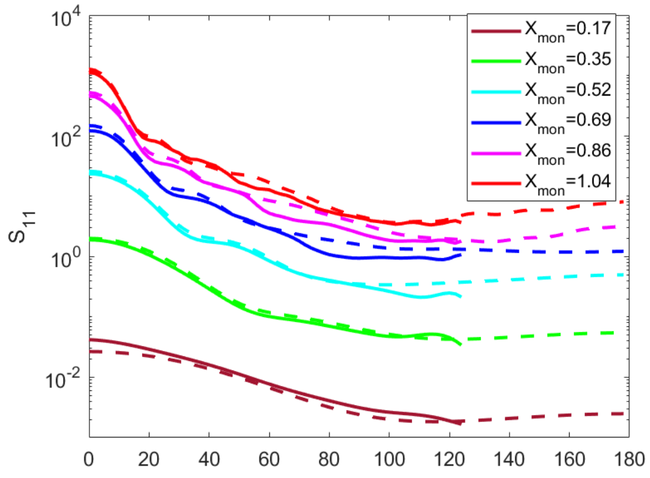

(a) Phase function

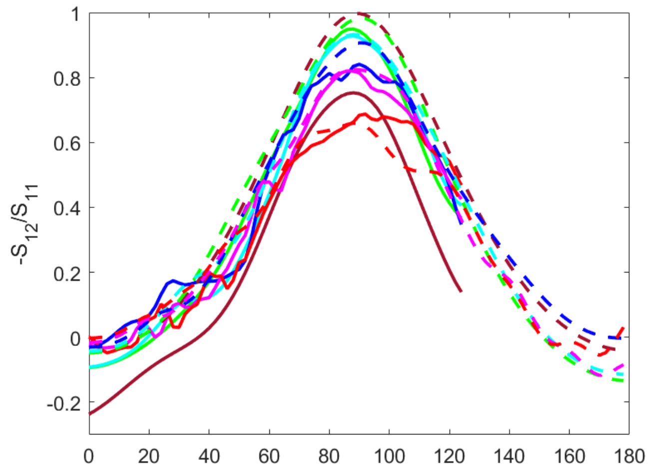

(b) Degree of linear polarization

Fig. 7. Measurements (solid lines) and simulations (dashed lines) of Ag_DLA_Df1.7_N74, from $X_{\mathrm{mon}} = 0.17$ to $X_{\mathrm{mon}} = 1.04$.

decreased compared to the wavelength, the scattering becomes almost isotropic, and, as a result, there is only the forward-scattering peak for the phase function. Additionally, DOP of Ag_DLA_Df2.8_N74 presents two main behaviors. The first one is a bell-shape, which illustrates that monomers are behaving like Rayleigh scatterers ($X_{\mathrm{mon}} = 0.17$ and $X_{\mathrm{mon}} = 0.35$). The second, is the oscillations, described as a pseudo-sphere behavior by Tazaki et al. (2016).

6.1.2. Effects of random positions of monomers in aggregates with the same fractal dimension

Figures D.1 and D.2 present the phase function and DOP of another two aggregates at $D_{\mathrm{f}} = 2$, which were generated using the same software and parameters ($N = 74$, $K_0 = 1.593$, $a_{\mathrm{int}} = a * 1.1$). However, as the software creates random positions of each monomer, each type of aggregate is completely unique. Comparing aggregates of this same fractal dimension, it is shown that even if all three aggregates were generated with different monomer configurations, phase function curves at the same X_{mon} present similar forward-scattering peaks and the same levels. The aggregate that has a little difference in terms of the width of the phase function forward-scattering peak is Ag_DLA_Df2.0_N74_1, compared to the other two aggregates. Moreover, DOP has a similar behavior as Ag_DLA_Df2.0_N74_1. In brief, all the aggregates of this same fractal dimension, two, present similar scattering properties, as can be seen in Fig. D.3 for the phase function.

To summarize Sect. 6.1, phase function of all aggregates (considering Figs. 4–8 and Appendix D) of different fractal dimensions and porosities presents a dominant forward scattering. As fractal dimension increases, coupling between monomers are going to be more important, and so we verified that at $D_{\mathrm{f}} > 2$ there is coupling represented on these bumps (named as multiple scattering by Berry & Percival 1986 and seen for $D_{\mathrm{f}} > 2$). This effect is also demonstrated with the DOP of Fig. 9, where the polarization is not only a contribution of the primary structure (monomer), but additionally there is an effect of depolarization that, we suggest, is due to coupling between monomers. Hence, among all aggregates, Ag_DLA_Df2.8_N74 presents the largest depolarization and

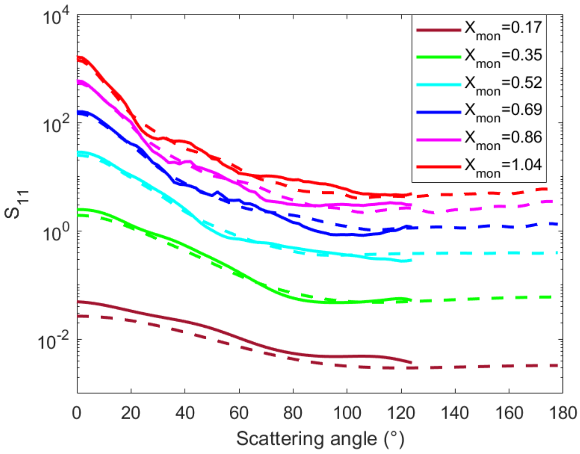

(a) Phase function

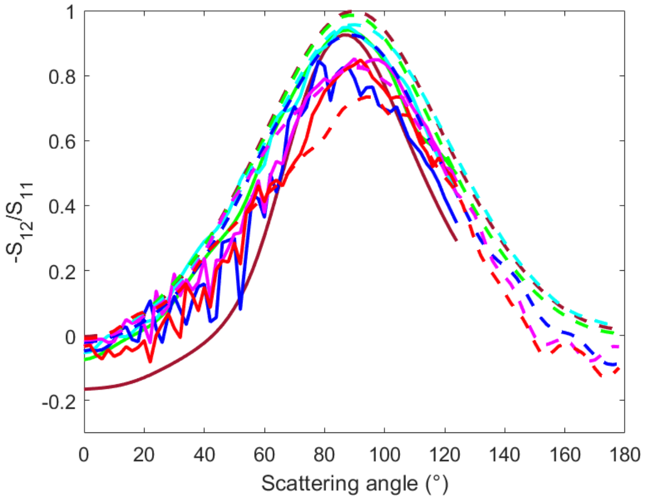

(b) Degree of linear polarization

Fig. 8. Measurements (solid lines) and simulations (dashed lines) of Ag_DLA_Df1.5_N74, from $X_{\mathrm{mon}} = 0.17$ to $X_{\mathrm{mon}} = 1.04$.

Ag_DLA_Df1.5_N74, the smallest. The monomer simulated with Mie does not present any depolarization. In other words, the aggregates presenting a higher porosity will have higher levels of DOP at $\theta = 100°$, while the less porous (Ag_DLA_Df2.8_N74 and Ag_DLA_Df2.5_N74) will have lower levels of DOP. This behavior was also seen by the simulations of amorphous silicate aggregates (refractive index of $1.689 + 0.0031i$ and $1.677 + 0.0044i$ at $\lambda = 0.45\ \mu\mathrm{m}$ and $0.65\ \mu\mathrm{m}$) containing $N = 2048$ in Halder et al. (2018), and it was related to different porosities using different types of aggregation, namely ballistic cluster agglomeration (BCCA), ballistic agglomeration (BA), and ballistic agglomeration with one and two migrations (BAM1 and BAM2).

On the other hand, at $X_{\mathrm{mon}} = 0.17$ (Fig. 10), all aggregates have a Rayleigh behavior for DOP as the monomer DOP, without any depolarization effects. Yet, the difference between the five fractal dimensions and the monomer is shown in the order of the phase function, the widest curve being $D_{\mathrm{f}} = 3.0$ (monomer) and the narrowest $D_{\mathrm{f}} = 1.5$ and $D_{\mathrm{f}} = 1.7$.

We suggest that when $X_{\mathrm{mon}} \ll 1$, the fractal dimension can be identified by the phase function width. On the other hand, when $X_{\mathrm{mon}} = 1$, depolarization in DOP can provide a notion of the fractal dimension.

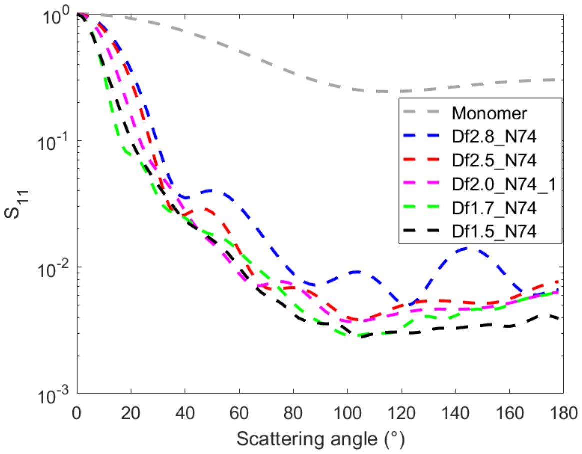

(a) Normalized phase function

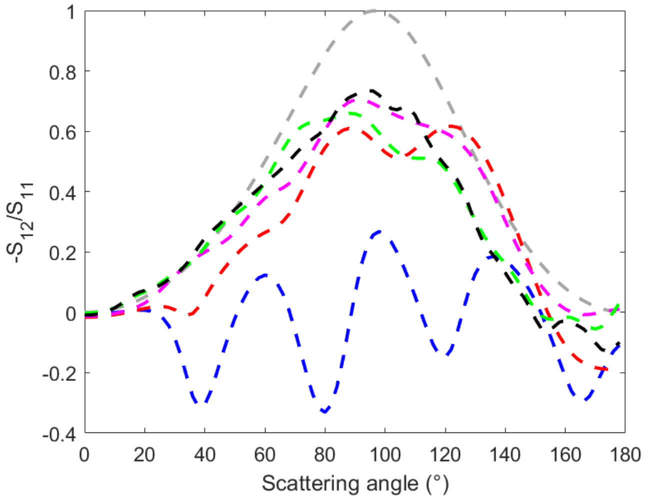

(b) Degree of linear polarization

Fig. 9. FEM simulations of five aggregates with different fractal dimensions at $X_{\mathrm{mon}} = 1.04$ and a Mie simulation for the monomer.

It should be noted that, in general, both scattering properties present a lot of resonance effects due to the fact that measurements and simulations are carried out for one object in multiple orientations, and not a distribution of sizes, which would minimize these oscillations. For this reason, future works focus on the analysis of these two scattering properties with a size distribution.

6.2. Angle at maximum DOP

Table 3 presents the angles at maximum DOP for all of the aggregates at the same six wavelengths, corresponding to six different X_{mon} for measurements and simulations. All values have at least an uncertainty of 2° due to the angular sampling.

The angles at maximum DOP should be analyzed at each X_{mon} for the different fractal size. For example, at $X_{\mathrm{mon}} = 0.17$ all aggregate results for simulated and measured maximum DOP are around 90°. However, at the other five size parameters, even if angles of maximum DOP are not too far from 90° there is a tendency of larger scattering angles for bigger

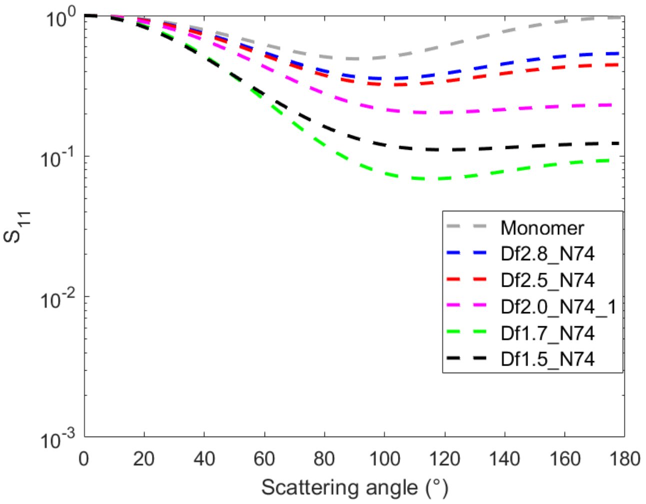

(a) Normalized phase function

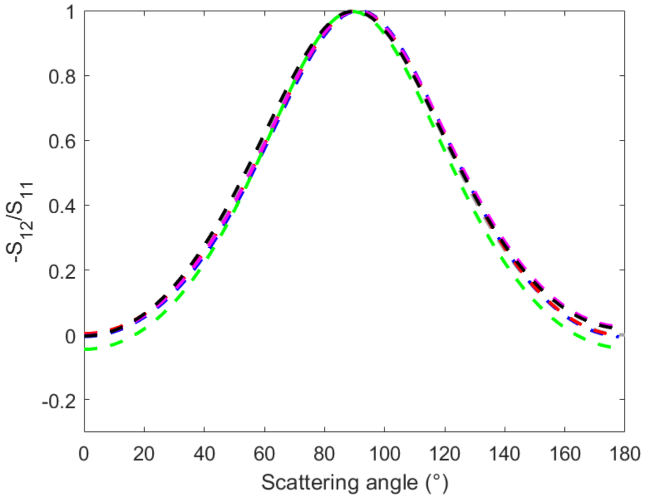

(b) Degree of linear polarization

Fig. 10. FEM simulations of five aggregates with different fractal dimensions at $X_{\mathrm{mon}} = 0.17$ and a Mie simulation for the monomer.

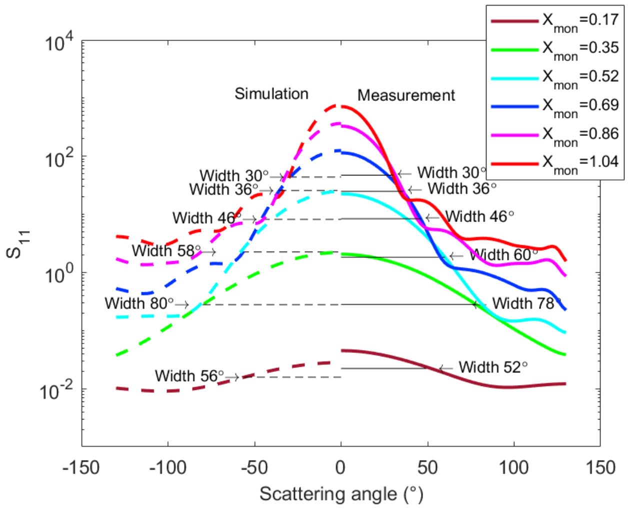

Fig. 11. Example of measured (solid lines) and simulated (dashed lines) HWHM of the phase function of Ag_DLA_Df2.5_N74.

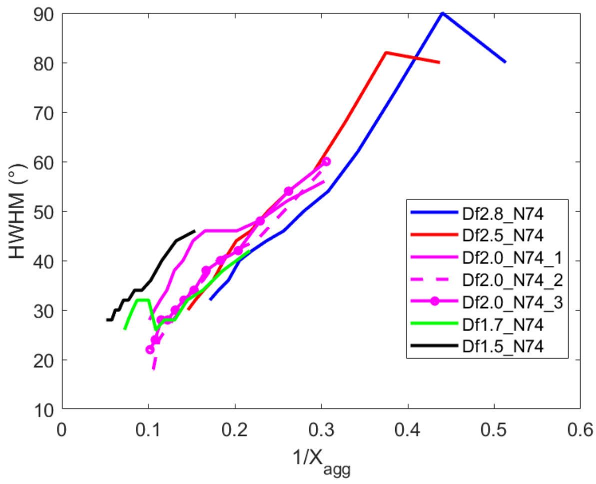

Fig. 12. Simulated HWHM of the phase function for all aggregates with their corresponding X_{agg}, from $\lambda = 50$ to 16.7 mm.

fractal dimensions ($D_{\mathrm{f}} = 2.8$ and 2.5) and smaller scattering angles for $D_{\mathrm{f}} = 1.5$. There is only one exception in which Ag_DLA_Df2.8_N74 has a smaller angle at $X_{\mathrm{mon}} = 0.52$ compared to Ag_DLA_Df1.5_N74. Based on the literature, DOP is mainly affected by monomers (Hadamcik et al. 2007, 2009, 2013), so knowing that all the aggregates had the same monomer size, we suppose that the difference from a big fractal dimension compared to a small fractal dimension is due to coupling effects. In other words, Ag_DLA_Df1.5_N74 has a DOP that is caused by monomers, while Ag_DLA_Df2.8_N74 has a DOP that is caused by monomers plus the coupling between them, making the difference of angles between small and big fractal dimensions.

6.3. Half width at half maximum of the phase function

Table 4 shows the evolution of half width at half maximum (HWHM) of the phase function of the seven aggregates at different X_{mon}. From $X_{\mathrm{mon}} = 0.35$ to 1.04, at each size parameter there is a decrease in the width, from the biggest to the smallest fractal dimension, which is the expected behavior because the forward-scattering peak width is inversely proportional to the size of the object. Thus, as the object becomes smaller, or at least its circumscribed sphere (from fluffy aggregates to compact aggregates), the forward-scattering peak becomes wider.

At $X_{\mathrm{mon}} = 0.17$, width values for all aggregates are around an average of 55.5° for measurements and 57.5° for simulations. This width is mainly due to the size of wavelengths compared to the sizes of aggregates (small aggregates compared to the wavelength present Rayleigh behaviors).

Another analysis that can be performed based on Table 4 is for each aggregate, studying how the width decreases at different X_{mon} from 0.35 to 1.04. For example, Ag_DLA_Df2.8_N74 has a measured HWHM from 78° (simulated 80°) to 32° (simulated 32°). All aggregates present this decrease because as wavelengths lowers, the size of the object compared to the wavelength is bigger, and so the forward-scattering peak will be narrowed. This effect is illustrated in Fig. 11 for the aggregate Ag_DLA_Df2.5_N74, comparing the simulation and measurements, and in Fig. 12, comparing all the aggregates' HWHM in terms of the inverse of aggregates size parameter, showing the linearity of this behavior.

Table 3. Angles at maximum DOP at different X_{mon} for different fractal dimensions.

X_{mon}/Ag_DLA	Df2.8_N74	Df2.5_N74	Df2.0_N74_1	Df2.0_N74_2	Df2.0_N74_3	Df1.7_N74	Df1.5_N74
0.17	92 (92)	90 (90)	88 (90)	88 (90)	92 (90)	88 (90)	86 (90)
0.35	104 (108)	96 (104)	92 (90)	88 (90)	86 (90)	88 (90)	88 (88)
0.52	62 (62)	124 (122)	92 (90)	90 (92)	88 (90)	88 (88)	88 (90)
0.69	102 (98)	90 (96)	90 (88)	84 (84)	88 (90)	90 (90)	78 (88)
0.86	124 (122)	106 (104)	100 (100)	90 (96)	92 (98)	86 (88)	90 (92)
1.04	102 (98)	90 (122)	94 (92)	94 (92)	90 (100)	92 (88)	92 (94)

Notes. Measured values (simulated values).

Table 4. HWHM of phase function at different X_{mon} for different fractal dimensions.

X_{mon}/Ag_DLA	Df2.8_N74	Df2.5_N74	Df2.0_N74_1	Df2.0_N74_2	Df2.0_N74_3	Df1.7_N74	Df1.5_N74
0.17	56 (54)	52 (56)	54 (58)	64 (62)	54 (60)	60 (58)	50 (54)
0.35	78 (80)	78 (80)	56 (56)	58 (58)	56 (60)	40 (42)	48 (46)
0.52	64 (62)	60 (58)	48 (46)	40 (42)	42 (42)	32 (32)	38 (36)
0.69	50 (46)	46 (46)	46 (44)	34 (34)	36 (34)	28 (26)	32 (32)
0.86	42 (40)	36 (36)	36 (34)	28 (26)	30 (28)	32 (32)	26 (30)
1.04	32 (32)	30 (30)	30 (28)	24 (18)	26 (22)	26 (26)	22 (28)

Notes. Measured values (simulated values).

7. Conclusions

The main conclusions of the present paper are summarized as follows:

1. The FEM simulation and measurement results of the phase function and DOP for all our of aggregates were consistent. Simulations and measurements for both scattering properties had similar behaviors and levels, proving a cross-validation.
2. All of our aggregates were generated and produced with the same refractive index, monomer size, and controlled geometry, being able to compare both scattering properties with constant parameters. Based on this, at $X_{\mathrm{mon}} = 0.17$, the phase function of all aggregates had the same shape of curve and level, showing a Rayleigh behavior at $\lambda = 100$ mm. This behavior was also proven by the maximum DOP at the same wavelength, presenting a value of ≈1 at 90° for all aggregates.
3. In general, the three aggregates having a $D_{\mathrm{f}} = 2$ presented a similar phase function. Their levels and forward-scattering peaks were very close, especially between Ag_DLA_Df2.0_N74_2 and Ag_DLA_Df2.0_N74_3.
4. At $X_{\mathrm{mon}} \ll 1$, the fractal dimension can be differentiated by the phase function width, while at $X_{\mathrm{mon}} = 1$, the differences of depolarization in DOP can provide a notion of this fractal dimension.
5. We verified that the maximum DOP of porous aggregates have higher levels at the same wavelength than for compact aggregates, as was already said in literature.
6. The maximum DOP presented a tendency: as the fractal dimension increased the value of the maximum was located at larger scattering angles, except at $X_{\mathrm{mon}} = 0.52$ for Ag_DLA_Df2.8_N74 and Ag_DLA_Df1.5_N74. We suggest that this tendency is due to coupling effects between the monomers of compact aggregates.
7. HWHM of the phase function presented larger values for compact aggregates and smaller values for fluffier aggregates, which is a normal effect based on the diffraction theory.

Without completely knowing which type of particles are present in protoplanetary disks, and based on later suggestions that there may be aggregates and irregular solid grains, our future works will focus on the study of particles with rough surfaces. This first study has provided a cross-validation between simulations and measurements, and so we will be able to measure other samples, such as these irregular grains without the necessity of using simulations. Indeed, scattering simulations of irregular solid grains are very difficult due to virtual meshing limitations being the only option laboratory measurements. Other perspectives are the study of the phase function and DOP with a size distribution of particles, and the correction of the calibration sphere at low frequencies.

Acknowledgement. This project was financially supported by CNRS, France, as part of its 80|PRIME cross-disciplinary programme. This work was also supported by the French National Research Agency in the framework of the Investissements d'Avenir program (ANR-15-IDEX-02), through the funding of the Cross-disciplinary Project "Origins of Life" of Univ. Grenoble-Alpes. The authors would like to thank the Centre de Transferts de Technologie du Mans (CTTM) for the impression of the 3D aggregates. We acknowledge Woźniak et al for providing the Diffusion Limited Aggregation software (DLA) that was used to generate aggregates (Wozniak et al. 2012). We would also like to thank "the Centre Commun de Ressources en Micro-Ondes" (CCRM) for providing the anechoic chamber and GDR Suie for the financial support. Finally, the anonymous reviewer of this paper is highly acknowledged for the comments and suggestions.

References

Amestoy, P. R., Duff, I. S., & L'Excellent, J.-Y. 2000, Comput. Methods Appl. Mech. Eng., 184, 501
Berry, M., & Percival, I. 1986, Optica Acta, 33, 577
Bertini, I., Gutierrez, P. J., & Sabolo, W. 2009, A&A, 504, 625
Blum, J. 2018, Space Sci. Rev., 214, 52
Bohren, C. F., & Huffman, D. R. 1983, Absorption and Scattering of Light by Small Particles (New York: John Wiley & Sons, Inc.), 544
Brownlee, D. E. 1979, Rev. Geophys. Space Phys., 17, 1735
Bucci, O. M., & Franceschetti, G. 1987, IEE Trans. Antennas Propag., AP-35, 1445
Draine, B. T., & Flatau, P. J. 1994, J. Opt. Soc. Am. A, 11, 1491
Draine, B. T., & Lee, H. M. 1984, ApJ, 285, 89

Eyraud, C., Geffrin, J. M., Litman, A., Sabouroux, P., & Giovannini, H. 2006, Appl. Phys. Lett., 89, 1
Eyraud, C., Sorsa, L.-I., Geffrin, J.-M., et al. 2020, A&A, 643, A68
Fraundorf, M. 1980, Stratospheric Brownlee particles: diverse leftovers from collapse, Tech. rep., NASA, Washington
Fulle, M., & Blum, J. 2017, MNRAS, 469, S39
Geffrin, J. M., García-Cámara, B., Gómez-Medina, R., et al. 2012, Nat. Commun., 3, 1171
Giese, R. H., Weiss-Wrana, K., Zerull, R. H., & Ono, T. 1978, A&A, 65, 265
Gustafson, B. Å. S. 1996, J. Quant. Spectrosc. Radiat. Transf., 55, 663
Gustafson, B. Å. S., & Kolokolova, L. 1999, J. Geophys. Res. Atmos., 104, 31 711
Güttler, C., Mannel, T., Rotundi, A., et al. 2019, A&A, 630, A24
Hadamcik, E., Renard, J. B., Levasseur-Regourd, A. C., & Worms, J. C. 2003, J. Quant. Spectrosc. Radiat. Transf., 79–80, 679
Hadamcik, E., Renard, J. B., Rietmeijer, F. J., et al. 2007, Icarus, 190, 660
Hadamcik, E., Renard, J. B., Levasseur-Regourd, A. C., et al. 2009, J. Quant. Spectrosc. Radiat. Transf., 110, 1755
Hadamcik, E., Renard, J. B., Mahjoub, A., et al. 2013, Earth Planets Space, 65, 1175
Halder, P., Deb Roy, P., & Das, H. S. 2018, Icarus, 312, 45
Kimura, H., Kolokolova, L., Li, A., & Lebreton, J. 2016, Light Scatter. Rev., 11, 363
Kolokolova, L., Hanner, M. S., Levasseur-Regourd, A.-C., & Gustafson, B. Å. S. 2004, in Comets II, ed. M. Festou, U. Keller, & H. Weaver (Tucson: Univ. of Arizona Press), 577
Lasue, J., & Levasseur-Regourd, A. C. 2006, J. Quant. Spectrosc. Radiat. Transf., 100, 220
Lasue, J., Levasseur-Regourd, A. C., Fray, N., & Cottin, H. 2007, A&A, 473, 641
Liu, L., & Mishchenko, M. I. 2018, Rem. Sens., 10
Mackowski, D. W., & Mishchenko, M. I. 1996, J. Opt. Soc. Amer. A, 13, 2266
Maconi, G., Helander, P., Gritsevich, M., et al. 2020, J. Quant. Spectrosc. Radiat. Transf., 246, 106910
Meakin, P. 1984, Phys. Rev. E, 29, 997
Merchiers, O., Geffrin, J. M., Vaillon, R., Sabouroux, P., & Lacroix, B. 2009, Appl. Phys. Lett., 94, 2
Merchiers, O., Eyraud, C., Geffrin, J.-M., et al. 2010, Opt. Express, 18, 2056
Min, M., Rab, C., Woitke, P., Dominik, C., & Ménard, F. 2016, A&A, 585, A13
Mishchenko, M. I. 2006, J. Quant. Spectrosc. Radiat. Transf., 101, 411
Mishchenko, M. I., Hovenier, J. W., & Travis, L. D., 2000, Light Scattering by Nonspherical Particles (San Diego: Academic Press), 690
Muñoz, O., Moreno, F., Guirado, D., et al. 2010, J. Quant. Spectrosc. Radiat. Transf., 111, 187
Muñoz, O., Moreno, F., Gómez-Martín, J. C., et al. 2020, ApJS, 247, 1
Renard, J. B., Worms, J. C., Lemaire, T., Hadamcik, E., & Huret, N. 2002, Appl. Opt., 41, 609
Renard, J. B., Hadamcik, E., Couté, B., Jeannot, M., & Levasseur-Regourd, A. C. 2014, J. Quant. Spectrosc. Radiat. Transf., 146, 424
Renard, J.-B., Geffrin, J.-M., Tobon Valencia, V., et al. 2021, J. Quant. Spectrosc. Radiat. Transf., 272, 107718
Sabouroux, P., Stout, B., Michel Geffrin, J., et al. 2007, J. Quant. Spectrosc. Radiat. Transf., 103, 156
Saleh, H., Charon, J., Dauchet, J., Tortel, H., & Geffrin, J. M. 2017, J. Quant. Spectrosc. Radiat. Transf., 196, 1
Schenk, O., & Gärtner, K. 2011, PARDISO, in Encyclopedia of Parallel Computing ed. D. Padua (Boston, MA: Springer US), 1458
Sorensen, C. M., & Roberts, G. C. 1997, J. Colloid Interface Sci., 186, 447
Sorensen, C. M., Heinson, Y. W., Heinson, W. R., Maughan, J. B., & Chakrabarti, A. 2017, Atmosphere, 8, 4
Sorensen, C. M., Yon, J., Liu, F., et al. 2018, J. Quant. Spectrosc. Radiat. Transf., 217, 459
Tazaki, R., & Tanaka, H. 2018, ApJ, 860, 79
Tazaki, R., Tanaka, H., Okuzumi, S., Kataoka, A., & Nomura, H. 2016, ApJ, 823, 1
Testi, L., Birnstiel, T., Ricci, L., et al. 2014, in Protostars and Planets VI, eds. H. Beuther, R. S. Klessen, C. P. Dullemond, & T. Henning (Tucson: University of Arizona Press) 339
Thomas-Osip, J. E., Gustafson, B. A. S., Kolokolova, L., & Xu, Y. L. 2005, Icarus, 179, 511
Vaillon, R., & Geffrin, J. M. 2014, J. Quant. Spectrosc. Radiat. Transf., 146, 100
Volten, H., Muñoz, O., Hovenier, J. W., et al. 2007, A&A, 470, 377
Voznyuk, I., Tortel, H., & Litman, A. 2015, IEEE Trans. Antennas Propag., 63, 2604
Wozniak, M., Onofri, F. R., Barbosa, S., Yon, J., & Mroczka, J. 2012, J. Aerosol Sci., 47, 12
Xu, Y. L., & Gustafson, B. Å. S. 1997, Appl. Opt., 36, 8026
Xu, Y. L., & Gustafson, B. Å. S. 2001, J. Quant. Spectrosc. Radiat. Transf., 70, 395
Zerull, R. H., Gustafson, B. Å. S., Schulz, K., & Thiele-Corbach, E. 1993, Appl. Opt., 32, 4088
Zubko, E., Shkuratov, Y., & Videen, G. 2015, J. Quant. Spectrosc. Radiat. Transf., 150, 42

Appendix A: Nonpolarized light

Based on the fact that Mueller elements are dimensionless values, if elements of both antipolar matrices were added (as shown in Equation A.3), that would produce nonpolarized matrix elements. Based on these elements, the phase function and DOP would be retrieved for nonpolarized light.

The Mueller matrix for emitter and receiver antennas in horizontal (||) polarization (parallel to the scattering plane) is presented in Equation A.1.

$$\begin{pmatrix} I_{\|s} \\ Q_{\|s} \\ U_{\|s} \\ V_{\|s} \end{pmatrix} = \frac{1}{k^2 r^2} \begin{pmatrix} S_{11} & S_{12} & S_{13} & S_{14} \\ S_{21} & S_{22} & S_{23} & S_{24} \\ S_{31} & S_{32} & S_{33} & S_{34} \\ S_{41} & S_{42} & S_{43} & S_{44} \end{pmatrix} \begin{pmatrix} 1 \\ 1 \\ 0 \\ 0 \end{pmatrix} = \frac{1}{k^2 r^2} \begin{pmatrix} S_{11} + S_{12} \\ S_{21} + S_{22} \\ S_{31} + S_{32} \\ S_{41} + S_{42} \end{pmatrix}. \tag{A.1}$$

The Mueller matrix for emitter and receptor antennas in vertical (⊥) polarization (perpendicular to the scattering plane) is described in Equation A.2.

$$\begin{pmatrix} I_{\perp s} \\ Q_{\perp s} \\ U_{\perp s} \\ V_{\perp s} \end{pmatrix} = \frac{1}{k^2 r^2} \begin{pmatrix} S_{11} & S_{12} & S_{13} & S_{14} \\ S_{21} & S_{22} & S_{23} & S_{24} \\ S_{31} & S_{32} & S_{33} & S_{34} \\ S_{41} & S_{42} & S_{43} & S_{44} \end{pmatrix} \begin{pmatrix} 1 \\ -1 \\ 0 \\ 0 \end{pmatrix} = \frac{1}{k^2 r^2} \begin{pmatrix} S_{11} - S_{12} \\ S_{21} - S_{22} \\ S_{31} - S_{32} \\ S_{41} - S_{42} \end{pmatrix}. \tag{A.2}$$

Adding equations A.1 and A.2, the resulting vector would give equation A.3.

$$\begin{pmatrix} I_{\|s} \\ Q_{\|s} \\ U_{\|s} \\ V_{\|s} \end{pmatrix} + \begin{pmatrix} I_{\perp s} \\ Q_{\perp s} \\ U_{\perp s} \\ V_{\perp s} \end{pmatrix} = \frac{1}{k^2 r^2} \begin{pmatrix} 2S_{11} \\ 2S_{21} \\ 2S_{31} \\ 2S_{41} \end{pmatrix}. \tag{A.3}$$

The elements of interest in order to calculate the phase function and DOP are S_{11} and S_{12}. Knowing that $S_{21} = S_{12}$ (based on Equation 6), we have the same elements, which give us the two scattering parameters of interest.

Equation A.3 proved that our measurements gave the same scale of values as if the source was nonpolarized light, and so it was possible to obtain the phase function (Equation 7) and DOP (Equation 8) for a nonpolarized source based on our polarized source measurements.

Appendix B: Simulation figures

The following figures are presented in support of different arguments that were presented and explained in Sections 3 and 5. Figure B.1 validates the reason why cross-polarized elements, S_3 and S_4, were not considered for other aggregate simulations and measurements of the phase function and DOP. It should be noted that the phase function has superposed curves, while the DOP including these two cross-polarized elements is affected at large X_{mon}. When the size of the aggregate and its monomers increase compared to the wavelength ($X_{mon} = 1.04$), the difference between cross-polarized elements increases, and thus so do DOP levels. For this reason, DOP including cross-polarization is more important than DOP with only co-polarized elements at large X_{mon} (Figure B.1.b dashed-dotted red line). Hence, depending on the threshold tolerance, S_3 and S_4 should be taken into account at large size parameters for future works on DOP. Additionally, Figure B.2 proved the accuracy between our two homemade codes: FEM and MoM.

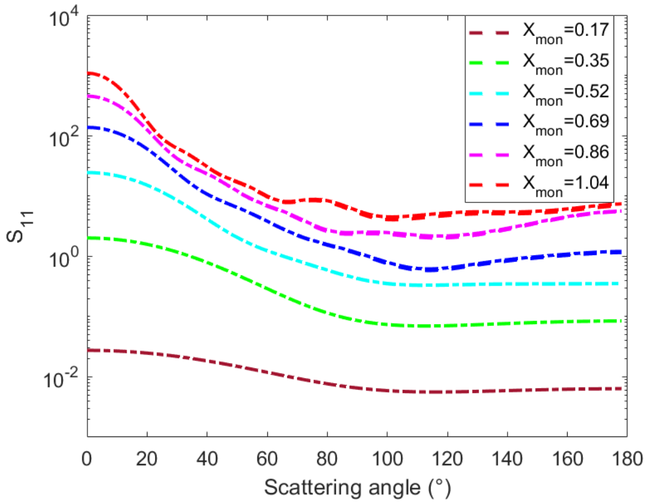

(a) Phase function

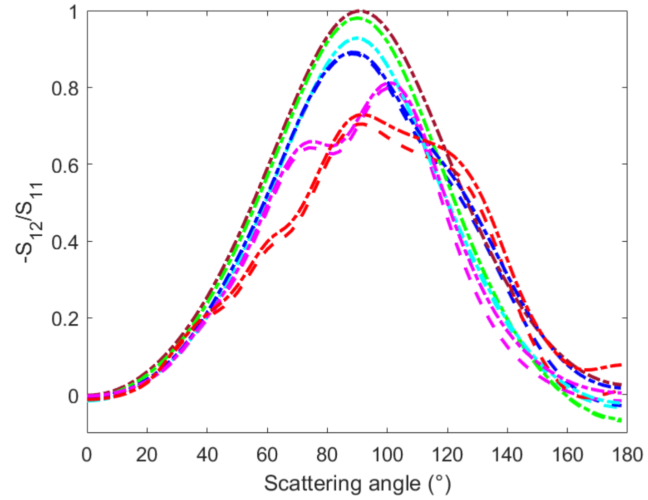

(b) Degree of linear polarization

Fig. B.1: FEM simulations of Ag_DLA_Df2.0_N74_1, considering co-polarized Jones matrix elements (dashed lines) and co-polarized plus cross-polarized elements (dashed-dotted lines), from $X_{mon} = 0.17$ to $X_{mon} = 1.04$.

Appendix C: Comparison criterion between measurements and FEM simulations

The following comparison criterion represents a way to estimate quantitatively the difference between our measurements and computations. This tool is important in order to compare both the validity of measurements and computations, and it will be used for our future works.

To estimate the difference between measurements and FEM simulations (either for the phase function or for the DOP) a root mean square deviation ($RMSD$) calculus was chosen, supposing the simulation as the reference. This criterion was normalized with the interquartile range (IQR), which is the difference between the 75th percentile ($Q3$) and the 25th percentile ($Q1$). Thus, the RMSD with the normalization is $RMSD_{IQR} = RMSD/(Q3 - Q1)$.

Furthermore, as the phase functions are represented with a logarithmic scale, this criterion is calculated on the logarithm of

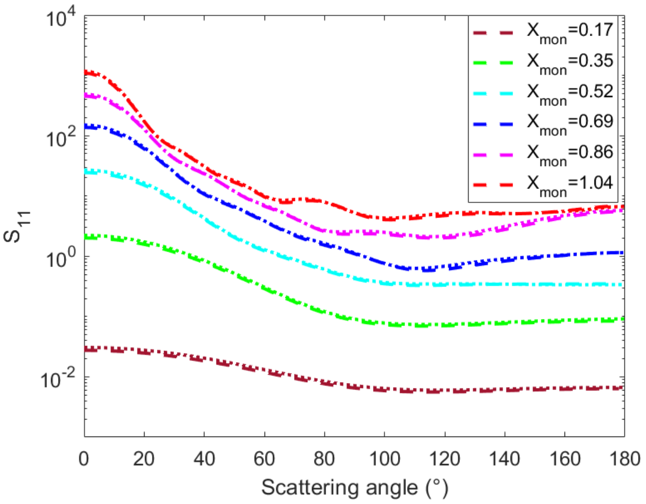

(a) Phase function

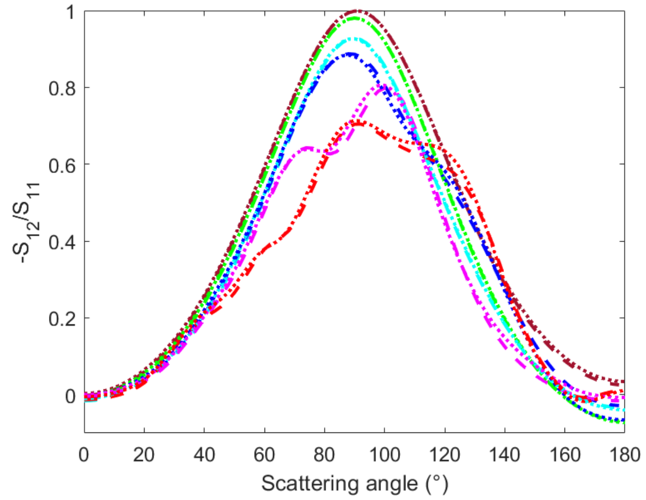

(b) Degree of linear polarization

Fig. B.2: FEM (dashed lines) and MoM (dotted lines) simulations, from X_{mon} = 0.17 to X_{mon} = 1.04 for Ag_DLA_Df2.0_N74_1 .

this quantity. The $RMS\,D_{IQR}$ is presented in Figure C.1 for the phase function and DOP of all aggregates.

The increasing values of the $RMS\,D_{IQR}$ obtained when the wavelength decreases (upper horizontal axis) are nothing but normal, but the higher values obtained at the larger wavelengths are due to two different phenomena. First, from an experimental point of view, the scattered signals are very low, and thus are more sensitive to noise (especially with the calibration target). Second, from a numerical point of view, the chosen box where the fields are computed begins to be too small for such large wavelengths. Both accuracies will be improved (treating large wavelengths separately, for example), but for this study, our aim was to work directly with the largest wavelength range possible.

Additionally, the gray line (in Figure C.1) represents the comparison between an exact calculus (Mie) of a solid sphere with a refractive index of 1.7 + i0.03 (same as aggregates) and the simulation of the same sphere with FEM. Thus, taking Mie computations as reference, the obtained criterion values give a good idea of the minimal values that may be obtained with such FEM computations.

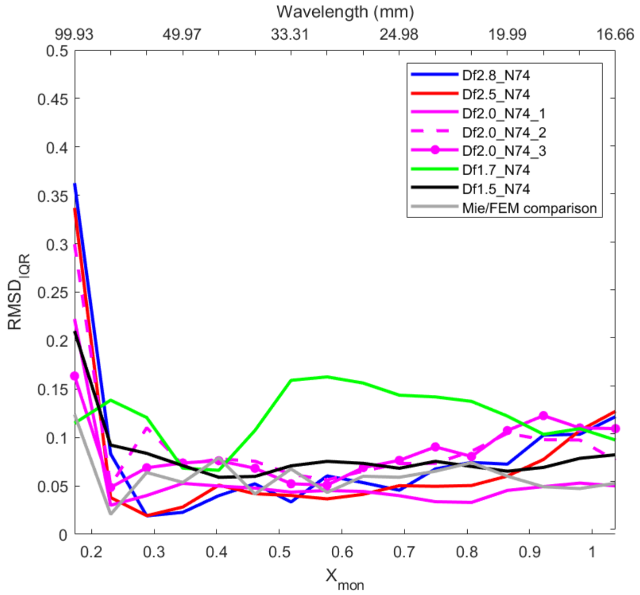

(a) $RMS\,D_{IQR}$ of the phase function

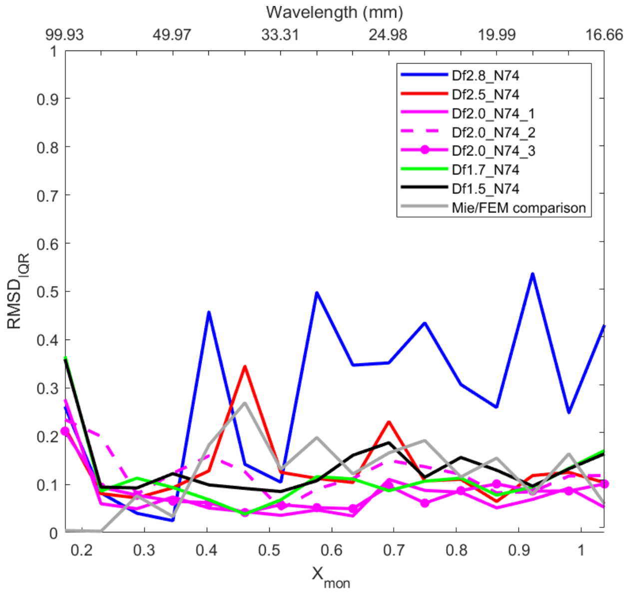

(b) $RMS\,D_{IQR}$ of the degree of linear polarization

Fig. C.1: Normalized root mean square deviations: a) on the log of the phase function; b) on the DOP, plotted for all the measured aggregates, taking their FEM simulation as reference. The gray line is a comparison of a Mie simulation versus a FEM computation (with a 32.5 mm diameter).

Appendix D: Other aggregate results at $D_f = 2$

Phase function and DOP of aggregates Ag_Df2.0_N74_2 and Ag_Df2.0_N74_3, in forward configuration and FEM simulations, are presented in Figures D.1 and D.2. Moreover, a phase function comparison of the three aggregates of fractal dimension two is shown in Figure D.3.

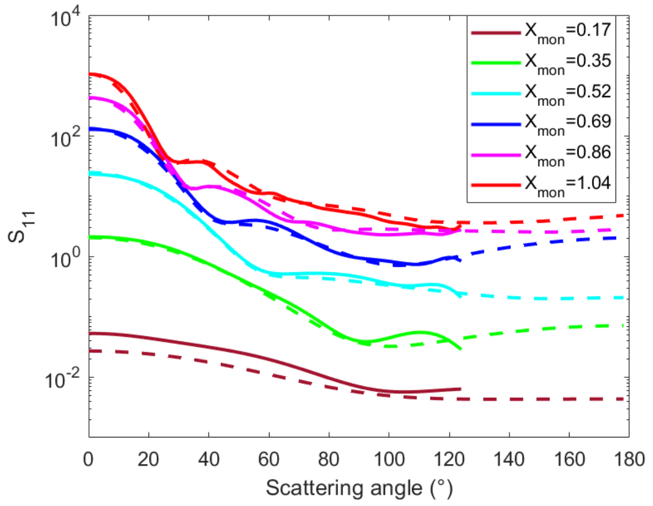

(a) Phase function

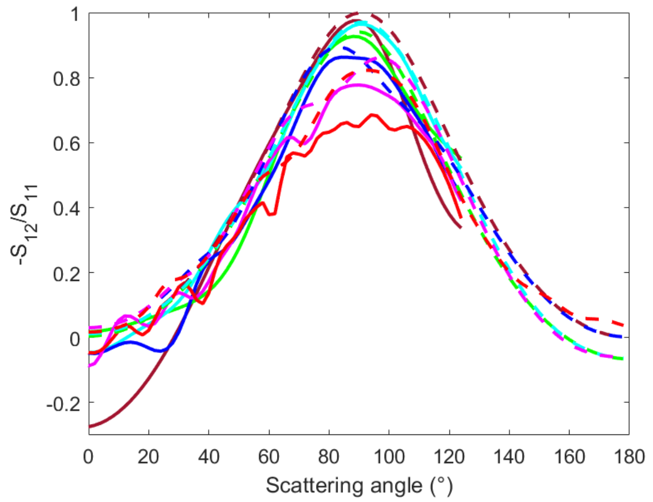

(b) Degree of linear polarization

Fig. D.1: Measurements (solid lines) and simulations (dashed lines) of Ag_DLA_Df2.0_N74_2, from X_{mon} = 0.17 to X_{mon} = 1.04.

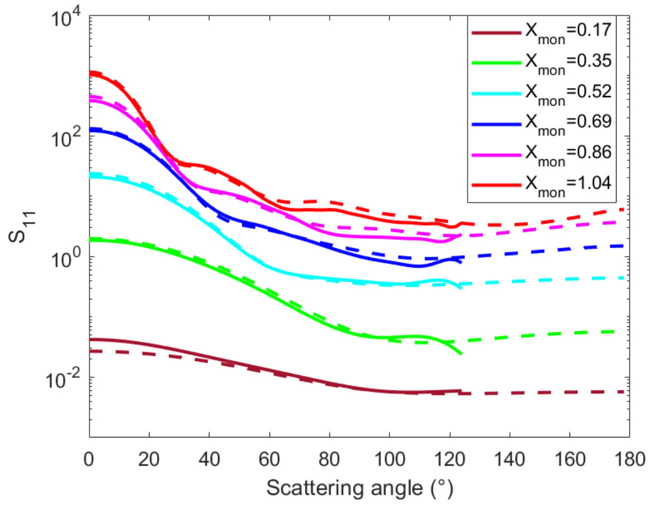

(a) Phase function

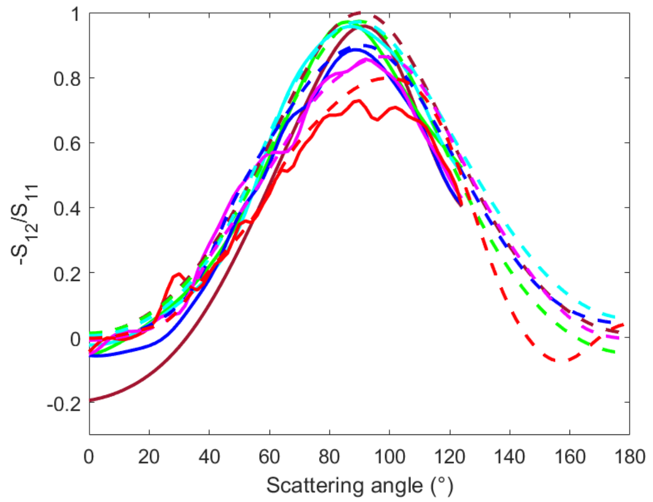

(b) Degree of linear polarization

Fig. D.2: Measurements (solid lines) and simulations (dashed lines) of Ag_DLA_Df2.0_N74_3, from X_{mon} = 0.17 to X_{mon} = 1.04.

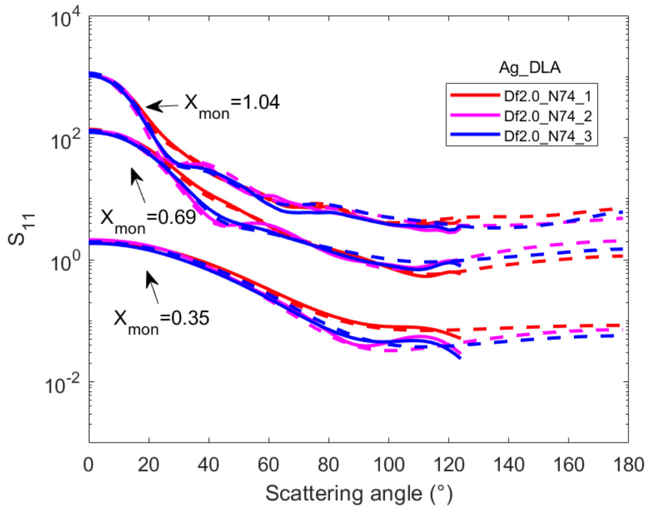

Fig. D.3: Measurements (solid lines) and simulations (dashed lines) of the scattering phase function for the three fractal aggregates at $D_f = 2$.